# A BIMODAL RECONSTRUCTION METHOD FOR BREAST CANCER IMAGING

## D. Flores-Tapia[1, 2, *], M. O'Halloran[3], and S. Pistorius[2, 4, 5]

[1]Department of Mathematics, University of Manitoba, Winnipeg, Manitoba R3T 2N2, Canada

[2]Division of Medical Physics, CancerCare Manitoba, Winnipeg, Manitoba R3E 0V9, Canada

[3]Department of Electrical and Electronic Engineering, National University of Ireland, Galway, Ireland

[4]Department of Physics & Astronomy, University of Manitoba, Winnipeg, Manitoba R3T 2N2, Canada

[5]Department of Radiology, University of Manitoba, Winnipeg, Manitoba R3E 0V9, Canada

**Abstract**—Breast Microwave Radar (BMR) has been proposed as an alternative modality for breast imaging. This technology forms a reflectivity map of the breast region by illuminating the scan area using ultra wide band microwave waveforms and recording the reflections from the breast structures. Nevertheless, BMR images require to be interpreted by an experienced practitioner since the location and density of the breast region can make the detection of malignant lesions a difficult task. In this paper, a novel bimodal breast imaging reconstruction method based on the use of BMR and Electrical Impedance Tomography (EIT) is proposed. This technique forms an estimate of the breast region impedance map using its corresponding BMR image. This estimate is used to initialize an EIT reconstruction method based on the monotonicity principle. The proposed method yielded promising results when applied to MRI-derived numeric breast phantoms.

## 1. INTRODUCTION

According to the American Cancer Society, approximately 1.3 million women will be diagnosed with breast cancer annually worldwide and 465,000 will ultimately die from the disease. [1]. As with many other types of cancer, early detection and medical intervention are crucial to the long-term survival of the patients. Currently, mammography is the gold standard for the detection of breast cancer. Although the use of this technology as a mass screening tool has led to a decrease in the mortality rates, it has a false positive rate between 60%–70% and a false negative rate of 10%–15% allowing significant room for improvement [2]. Ultrasound (US) and Magnetic Resonance Imaging (MRI) have been introduced to provide a more accurate diagnosis. Nevertheless, MRI is not cost effective and US images are difficult to interpret [2].

During the last 10 years, there has been a widespread interest in the breast imaging community regarding the use of Electromagnetic Imaging (EMI) techniques [3–6]. These technologies take advantage of the impedance differences between normal and malignant tissues in the 10 KHz–10 GHz frequency range [7–10]. Compared to x-ray mammography, EMI techniques are safer and less stressful for the patient since no ionizing radiation is used and the breast is not compressed during the imaging process. One promising EMI technique is Breast Microwave Radar (BMR) [6, 11]. This modality records the reflections from the breast structures when the breast region is illuminated by an Ultra Wide Band (UWB) electromagnetic wave. The collected signals are then processed to form a reflectivity map of the breast. Two recent studies [6, 11] have shown the feasibility and potential of BMR as a breast imaging method. The results of these studies indicate that BMR has the potential to detect malignant lesions of at least 4 mm and can generate 3D reflectivity maps [6].

Although the feasibility of BMR has been assessed in recent studies, this technology still present limitations that prevents its widespread use in clinical environments. The most significant challenge that BMR imaging faces are the effects of the dense tissue structures in the breast region [6, 11–13]. Recent experimental studies have shown that these regions have conductivity and permittivity values that significantly limit the propagation of UWB signals used in BMR imaging [14, 15]. Furthermore, fibroglandular structures also produce strong reflections that can potentially be mistaken for breast lesions in reconstructed BMR images [14, 15]. These effects make the detection of lesions that are attached or close to a dense tissue structure a challenging task [14, 15], and may lead to a decrease in specificity as

the density of the breast region increases. Since 80% of all breast cancers are invasive ductal carcinomas (which start at fibroglandular regions), several techniques have been proposed to differentiate tumors from dense tissue region sin BMR images [16–18]. The majority of these methods are based on the use of contrast agents that enhance the contrast between malignant lesions and dense tissue structures. Nevertheless, similar to other contrast agent-based imaging modalities, further work is necessary to assess the absorption and diffusion rates of the agents among the different kinds of tissues in the breast to establish a suitable imaging protocol.

An alternative approach is the joint use of BMR and tomographic EMI modalities. Tomographic EMI techniques generate an impedance (or conversely admittance) distribution map of the breast region, in which the presence of malignant lesions can be quantitatively assessed [3–5, 19–23]. A recent study has shown that multi modality EMI approaches have an increased sensitivity and sensibility compared to individual EMI techniques [3]. However, the detection of non palpable tumors (smaller than 1 cm) using current tomographic EMI reconstruction techniques is a difficult task since these approaches generate images with diffused edges and where only targets with sizes in the order of centimeters can be resolved [3].

In this paper, a novel multimodal EMI image formation technique is proposed. This approach uses BMR and Electrical Impedance Tomography (EIT) methods to form a conductivity map of the scan region. The BMR images are processed to extract the location of the tissue boundaries in the breast region and form an initial estimate of the resistivity distribution of the scan region. Since the reflected waves are caused by the interfaces between the different kinds of tissues in the in the breast region (fatty, fibroglandular and tumors), BMR images provide the location of the boundaries between different breast areas. Next, this information is used to initialize a novel EIT reconstruction process based on the monotonicity principle [24]. This EIT reconstruction approach forms a resistivity map of the conducting domain without iteratively solving a series of forward problems. In this methodology, the ill posed nature of the inverse EIT problem can be compensated by making use of known physical properties of the object being imaged [7]. Monotonicity methods have a number of features that make their use in a clinical environment quite attractive, such as robustness in the presence of noise [24]. The work in this paper extends the preliminary results presented by the authors in [25] in two key aspects. Firstly, it provides a more detailed mathematical analysis of the monotonicity principle applied in breast imaging scenarios. Secondly, the validation is performed using breast phantoms with a

significantly higher amount of fibroglandular tissue and where the malignant lesions are attached to the dense tissue structures. The proposed method is capable of producing spatially accurate images with defined edges where the malignant lesions can be distinguished.

This paper is organized as follows: A brief description of the BMR wavefront reconstruction methodis given in Section 2. In Section 3, the principles of EIT reconstruction using a monotonicity approach are explained; the proposed method is then described in Section 4. A series of reconstructed images obtained using numeric test beds are shown in Section 5. Finally, some concluding remarks are addressed in Section 6.

## 2. BMR WAVEFRONT RECONSTRUCTION

BMR images are created by illuminating the breast region with a UWB waveform from a predefined scan geometry that is parallel to the breast surface. At each location a waveform $f(t)$ with a bandwidth $W$, is irradiated and the responses from the structures within the scan area are recorded. BMR models the breast structures as a set of point scatters where each one has a specific reflectivity value.

A 2D cylindrical scan geometry is considered in this paper, in which the scan process is performed along a series of circular trajectories in the $(x, y)$ plane with a radius $R$. This geometry was chosen due to its ability to generate a high SNR images and to achieve a spatial resolution in the order of millimeters [26]. In cylindrical scan geometries, the antennas are facing towards the center of the circular trajectory at all scan locations. A total of $Q$ point scatters are assumed to be inside the scan region. In the following discussion, a polar coordinate system is used to simplify the calculations, with $M$ planes in which each scan plane has $N$ scan locations. For the scan element located at $(R, \theta)$, where $\theta$ is the angular position, the received signal can be expressed as:

$$s(t,\theta) = \Sigma_{q=1}^{T} \vartheta_q f\left(t - \frac{2 \cdot L_q(\theta)}{\upsilon}\right) \tag{1}$$

where $\upsilon$ is the medium propagation, $\vartheta_q$ is the reflectivity of the $q$th scatter, $L_q(\theta)$ is the distance between the scan location at $(R, \theta)$ and the $q$th scatter given by:

$$L_q(\theta) = \sqrt{R^2 + r_q^2 - 2 \cdot R \cdot r_q \cos(\phi_q - \theta)} \quad \text{for } \theta \in [0, 2\pi] \tag{2}$$

and $r_q = \sqrt{x_q^2 + y_q^2}$, $\phi_q = \tan^{-1}(y_q/x_q)$ and $(x_q, y_q)$ is the location of the $q$th scatter.
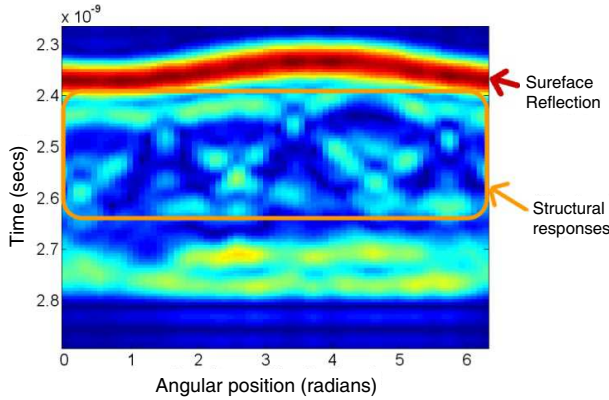
**Figure 1.** Unprocessed BMR dataset.

Breast structures in BMR data sets present nonlinear signatures due to the different signal travel times along the different scan locations [7] and the near field distances between the targets and the scan geometry. As illustrated in Figure 1, it is difficult to assess the locations and dimensions of the targets present in the scan area. To properly assess the target dimensions and locations, the data must be reconstructed. An effective way of doing this is by using the wavefront reconstruction approach proposed in [13, 27]. This method compensates the spectrum of the recorded responses by removing the effects of the scan geometry. The first step is to calculate the Fourier transform of the spherical phase function along the $z$ and $\theta$ directions. This operation is given by:

$$S_p(\omega, \zeta) = \int_0^{2\pi} \sigma_p \cdot F(\omega) \cdot \exp(-j(2k \cdot L_p(\theta, z) + \zeta\theta))d\theta \qquad (3)$$

where $\zeta$ is the spatial frequency counterparts of $\theta$. After $S_p(\omega, \zeta)$ is determined, by using the mathematical procedure described in [7] the compensated spectrum with the following form will be obtained:

$$\begin{aligned} U_p(\omega, \zeta) &= 4\vartheta_p \cdot \xi_p(\omega, \zeta) \cdot \exp\Big(-j\Big(\sqrt{4k^2r_p^2 - \zeta^2} \\ &\quad + \zeta \cdot \sin^{-1}(\zeta/2kr_p) + \zeta\phi_p\Big)\Big) \end{aligned} \qquad (4)$$

where $k = \omega/\nu$. The next step is to transfer the data in $U_p(\omega, \zeta)$, from the $(\omega, \zeta)$ frequency space to the $(k_x, k_y)$ spatial frequency space, where $k_x$ and $k_y$ are the spatial frequency counterparts of $x$ and $y$ spatial domains. This is achieved by first calculating the inverse FFT of the focused data in the $\zeta$ direction, resulting in a representation of

the collected data in the $(k, \theta)$ domain. We will refer to the resulting spectrum as $U_p(k, \theta)$. According to the Fourier slice theorem, $S(\omega, \theta)$ corresponds to a set of $N$ equally spaced projections of the rectangular frequency spectrum, $I(k_x, k_y)$. Each projection passes through the origin and has the same angle as the scan location where it was recorded. By using this property, $U_p(k, \theta)$ can be transferred into a rectangular coordinate system using the following mapping:

$$k_{ux} = k \cdot \cos(\theta) \tag{5}$$
$$k_{uy} = k \cdot \sin(\theta) \tag{6}$$

This new mapped spectrum will be denoted as $I_p(k_{ux}, k_{uy})$. The differences between adjacent samples in the $(k_{ux}, k_{uy})$ plane are not constant, resulting in an unevenly sampled frequency space. In order to obtain a uniformly sampled spectrum, a new discrete frequency space, denoted as $(k_x, k_y)$, is defined. In this space the separation between samples in each $(k_x, k_y)$ plane is $\Delta k_y = \Delta k_x = \pi/R$. Next, the evenly sampled spectrum $I_p(k_x, k_y)$, is generated by interpolating the data contained in $I_p(k_{ux}, k_{uy})$ into the frequency values specified in the $(k_x, k_y)$ space. Finally, to visualize the reconstructed data in the spatial domain, a 2D inverse FFT is applied to $I_p(k_x, k_y)$. The result of this process is the image $i_p(x, y)$. A more detailed explanation of the cylindrical BMR holographic reconstruction technique is given in [13].

## 3. THE MONOTONICITY PRINCIPLE

Consider a 2D observation domain, $D$, formed by an ohmic material with an impedivity given by $z(x, y, \omega) = \rho(x, y, \omega) + j \cdot \psi(x, y, \omega)$, where $\rho(x, y, \omega)$ and $\psi(x, y, \omega)$ denote the electrical resistivity and reactivity respectively. The observation domain is accessible by means of a finite number, $M$, of electrodes located at its boundary. The measurement protocol can be described as follows. A current pattern of the form $A \cdot \cos(\omega t)$ is injected between the first and the $M$th electrodes. Next the potential difference between the $k$th, where $k = 1, 2, 3 \ldots, M - 1$, and the $M$th electrodes are measured. The field equations that model the conduction in $D$ are given by:

$$\nabla \times E = 0 \quad \text{in } D \tag{7}$$
$$\nabla \cdot J = 0 \quad \text{in } D \tag{8}$$
$$z(x, y, \omega) J(x, y, \omega) = E(x, y, \omega) \quad \text{in } D \tag{9}$$
$$J \cdot n = 0 \quad \text{on } S_\perp \tag{10}$$
$$E \times n = 0 \quad \text{on } S_1 \cup S_2 \cup \ldots S_{M-1} \tag{11}$$
$$\int_{\gamma k} E \cdot dl = v_k \quad k = 1, 2, \ldots, M - 1 \tag{12}$$

$$\int_{S_k} J \cdot n dS = i_k \quad k = 1, 2, \ldots, M - 1 \tag{13}$$

where $S_k$ is the part of the boundary $S = \partial D$ in contact with the $k$th electrode, $S_\perp$ is the part of $S$ in contact with the host medium, $n$ is the normal component to $S$, $\gamma_k$ is a line contained in $D$ connecting the $k$th and the $M$th electrodes, $i_k$ is the current at the $k$th electrode, and $v_k$ is the voltage difference between the $k$th and the $M$th electrodes. This process is then repeated for the $M - 1$ electrodes surrounding $D$. In this data acquisition protocol, the $M$th is always grounded and all the voltage measurements are made with respect to this reference.

The relationship between the injected currents and the measured voltages is given by:

$$V = Z_D I \tag{14}$$

where $I = [i_1, i_2, i_3, \ldots, i_{M-1}]^T$, $V = [v_1, v_2, v_3, \ldots, v_{M-1}]^T$, and $Z_D$ is known as the impedance matrix. The power dissipated by $D$ is given by:

$$\int_D E \cdot J dr = I \cdot Z_D \cdot I^T = \int_D \rho(x, y, \omega) + j \cdot \psi(x, y, \omega) \|\nabla \times T\|^2 dxdy \tag{15}$$

The real part of (15) can be expressed as follows:

$$Re\left(I \cdot Z_D \cdot I^T\right) = \iint_D \rho(x, y, \omega) \|\nabla \times T\|^2 dxdy \tag{16}$$

where $T$ is the electric vector potential. The variational characterization of the real components of the problem described in Equations (11)–(16) can be described in terms of the electric scalar and vector potentials as follows:

$$\text{find } \varphi \in \Phi^v \quad \text{minimizing} \quad \iint_D \sigma(x, y) \|\nabla \varphi\|^2 dxdy \tag{17}$$

$$\text{find } T \in A^l \quad \text{minimizing} \quad \iint_D \rho(x, y) \|\nabla \times T\|^2 dxdy \tag{18}$$

where $\sigma(x, y) = \rho(x, y)/((\rho(x, y, \omega))^2 + (\psi(x, y, \omega))^2)$ :

$$\Phi^v \triangleq \left\{ \varphi' \in \phi | \varphi'|_{S_{M+1}} = 0, \quad \varphi'|_{S_k} = v_k, \quad k = 1, 2, 3, \ldots, M \right\} \tag{19}$$

$$A^l \triangleq \left\{ H' \in A | \int_{S_k} \nabla \times T' \cdot n ds = i_k, \quad k = 1, 2, 3, \ldots, M \right\} \tag{20}$$

$$\Phi \triangleq \left\{ \varphi' \in L_{grad}^2(D) | n \times \nabla \varphi' = 0 \text{ on } S_1 \cup S_2 \cup \ldots \cup S_{M+1} \right\} \tag{21}$$

$$A \triangleq \left\{ H' \in L_{rot}^2(D) | n \cdot \nabla \times T' = 0 \text{ on } S_\perp \right\} \tag{22}$$

$$L_{grad}^2(D) \triangleq \left\{ \varphi' \in L^2(D) | \nabla \varphi' \in L^2(D) \right\} \tag{23}$$

$$L_{rot}^2(D) \triangleq \left\{ a \in L^2(D) | \nabla \times a \in L^2(D) \right\} \tag{24}$$

EIT reconstruction approaches form an impedance (or admittance) distribution map of the scan region based on the boundary measurements. Currently, the most common methodology to reconstruct EIT images is by using nonlinear iterative reconstruction techniques [28–32]. Iterative methods perform a nonlinear optimization process in which finite element solutions are iteratively generated to minimize a predefined cost function between the measured electrode surface currents and those predicted by the model, as the estimated property distribution is changed [28, 29, 31, 32]. The potential solutions are generated using a Finite Element Modeling (FEM) approach in which the Laplace equation is commonly used to model the EIT forward problem. These techniques perform a regularization process to compensate the ill-posed nature of the EIT inverse problem. Although iterative approaches represent the state of the art to solve non-linear inverse problems, they require the solution of the direct problem for several assigned tentative shapes of the inclusion and can be very expensive in terms of computer time [24]. Moreover, the convergence cannot be guaranteed [24].

An alternative method to form EIT images is by using direct reconstruction methods, such as the D-bar, linear modeling, and strip line just to mention a few [24, 33–35]. These approaches form a distribution map of the conducting domain without iteratively solving a series of forward problems. Direct reconstruction compensate for the ill posed nature of the inverse EIT problem by making use of known physical properties of the object being imaged. This is the equivalent of the regularization procedure, which can also be considered as a way to utilize *a priori* information about the electric characteristics of the scan region in the reconstruction process, since the regularization used by iterative approaches should favor known physical properties of the target [24, 29].

In this paper, a direct approach based on the monotonicity principle is used [24]. This methodology relies on the monotonicity of the map $(x, y) \mapsto Re(Z_D)$. This approach was chosen because it is extremely resilient to noise and requires a smaller number of boundary measurements than conventional direct methods resulting in a robust convergence criterion [24]. The monotonicity principle can be described as follows. Consider two different domains, $D_1$ and $D_2$, where $\rho_1(a) > \rho_2(a)$ and $\psi_1(a) < \psi_2(a)$ where $a$ is a particular location.

If the current vector is fixed, from (18), it can be shown that:

$$
\begin{aligned}
Re\left(I \cdot Z_{\rho 1} \cdot I^T\right) &= \iint\limits_{D_1} \rho_1(x,y)\|\nabla \times T_1\|^2 dxdy \\
&\geq \iint\limits_{D_2} \rho_2(x,y)\|\nabla \times T_1\|^2 dxdy \\
&\geq \iint\limits_{D_2} \rho_2(x,y)\|\nabla \times T_2\|^2 dxdy \\
&= Re\left(I \cdot Z_{\rho 2} \cdot I^T\right)
\end{aligned}
\tag{25}
$$

where $T_1$ and $T_2$ are the electric vector potentials corresponding to $D_1$ and $D_2$. Therefore $Re(Z_{\rho 1}) \geq Re(Z_{\rho 2})$. Next, consider a conduction domain $D_\Omega$ defined as:

$$
D_\Omega(x,y) = \begin{cases} \rho_h + j \cdot \psi_h & \text{for } (x,y) \in D_\Omega(x,y) \setminus \Omega \\ \rho_\Omega + j \cdot \psi_\Omega & \text{for } (x,y) \in \Omega \end{cases}
\tag{26}
$$

where $\Omega$ is perfectly conducting inclusion within $D_\Omega(x,y)$, $\rho_\Omega + j \cdot \gamma_\Omega$ and $\rho_h + j \cdot \gamma_h$ are the impedivity of the inclusion and the background respectively. Additionally:

$$
0 = \rho_\Omega < \rho_h \ll \infty
\tag{27}
$$
$$
0 < \psi_h < \psi_\Omega \ll \infty
\tag{28}
$$

$\bar{\Omega}_c$, the closure of $\Omega$, is not in contact with any electrodes. A graphical illustration of $D_\Omega(x,y)$ can be seen in Figure 2(a). Using the monotonicity principle, it can be shown that for an inclusion $\Omega_1$:

$$
\Omega_1 \subseteq \Omega \Rightarrow Re(Z_\Omega) \leq Re(Z_{\Omega_1})
\tag{29}
$$

from:

$$
\begin{aligned}
Re\left(I \cdot Z_\Omega \cdot I^T\right) &= \iint\limits_{D_\Omega \setminus \Omega} \rho(x,y)\|\nabla \times T_\Omega\|^2 dxdy \\
&\leq \iint\limits_{D_{\Omega_1} \setminus \Omega} \rho(x,y)\|\nabla \times T_\Omega\|^2 dxdy \\
&= \iint\limits_{D_{\Omega_1} \setminus \Omega} \rho(x,y)\|\nabla \times T_{\Omega_1}\|^2 dxdy \\
&= Re\left(I \cdot Z_{\Omega_1} \cdot I^T\right)
\end{aligned}
\tag{30}
$$
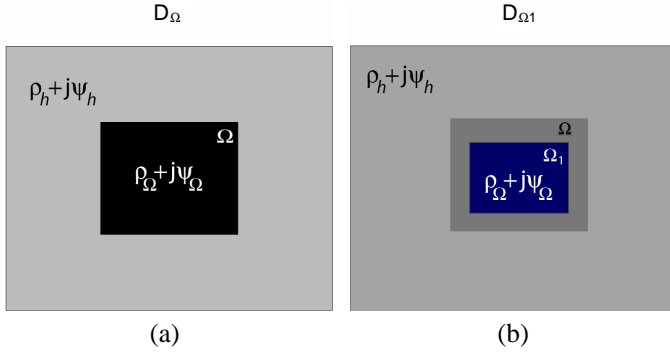
**Figure 2.** 2D inclusion example. (a) $D_\Omega(x,y)$. (b) $D_{\Omega_1}(x,y)$.

where:

$$D_{\Omega_1}(x,y) = \begin{cases} \rho_h + j \cdot \psi_h & \text{for } (x,y) \in h \setminus \Omega_1 \\ \rho_\Omega + j \cdot \psi_\Omega & \text{for } (x,y) \in \Omega_1 \in \Omega \end{cases}, \tag{31}$$

$Z_\Omega$ and $Z_{\Omega_1}$ are impedance matrices corresponding to $D_\Omega(x,y)$ and $D_{\Omega_1}(x,y)$, the simulated dataset containing $\Omega_1$, and $T_\Omega$, $T_{\Omega_1}$ are the corresponding electric vector potentials of these datasets. The first and last lines follow from the definition of impedance matrix, the second line from $\nabla \times T_\Omega \geq 0$ in $\Omega \supset \Omega_1$ and the third line from $T_\Omega \in A_\Omega^l \subset A_{\Omega_1}^l$. The relation $Re(Z_\Omega) \leq Re(Z_{\Omega_1})$ can be determined by evaluating if the sign of $Re(Z_\Omega) - Re(Z_{\Omega_1})$ is negatively well defined respectively. Figure 2(b) has an illustration of $D_{\Omega_1}(x,y)$. A more detailed proof can be found in [24].

In practice, the value resistivity value of $\Omega$ will likely be greater than 0, which can result in an overestimation of the inclusion dimensions. To avoid this, a two phase reconstruction procedure is performed as follows. Lets model $D_\Omega$ as the union of individual non overlapping elements $\tau_1, \tau_2, \ldots \tau_T$ with equal dimensions. A set of test matrices $Z_{\Omega_{\tau_n}}$ is then generated to assess the presence of an inclusion in the conducting domain. If the sign of $Re(Z_\Omega) - Re(Z_{\Omega_{\tau_n}})$ is negatively well defined, then $\Omega_{\tau_n} \subseteq \Omega$. A matrix is negatively well defined if the sign index, denoted as $s_n$, is equal to $-1$. The sign index is defined as:

$$s_n = \frac{\Sigma_{j=1}^T \lambda_{\tau_n,j}}{\Sigma_{j=1}^T |\lambda_{\tau_n,j}|} \tag{32}$$

where $\lambda_{\tau_n,j}$ is the $j$th eigenvalue of $Re(Z_\Omega) - Re(Z_{\Omega_{\tau_n}})$ and $T$ is the total number of eigenvalues in the difference matrix.
Next, a second step is performed to eliminate the residual areas in this initial estimate, denoted as $\Omega_{ext}$. In this procedure, the sign

of $Re(Z_\Omega) - Re(Z_{\Omega_{ext\backslash\tau_n}})$ is evaluated, where $\Omega_{ext} = \cup_{n=1}^N \tau_n$. If the corresponding sign index is negatively well defined then $\Omega_n$ is not part of $\Omega$ [24]. Similarly to the previous step, this process is repeated for all the $Z_{\Omega_{ext\backslash\tau_n}}$ scenarios. The reconstructed inclusion, $\Omega_{int}$, is then assembled using all the spatial components of the candidate matrices corresponding sign is not negative well defined ($s_n > -1$). This same analysis holds for scenarios where:

$$0 < \rho_h < \rho_\Omega = \infty \tag{33}$$
$$0 < \psi_\Omega < \psi_h \ll \infty \tag{34}$$

In this case, $\Omega_{\tau_n} \subseteq \Omega \Rightarrow Re(Z_\Omega) \le Re(Z_{\Omega_{\tau_n}})$, the criteria for sign of the matrix subtraction should be positively well defined, which is indicated if and only if $s_k = 1$. A more detailed explanation of the theoretical framework behind the monotonicity principles given in [24].

## 4. METHODOLOGY

### 4.1. The Electric Properties of Breast Tissues

The interior of a healthy breast region can be considered to be formed primarily by two main types of tissues: fatty and fibroglandular. The average proportion of these tissues in an average breast region is $70 : 30$ [36]. During the last three decades, several research groups have measured the electric properties of the different breast tissues. The latest studies suggest that the admittance of cancer tissues have an average contrast of at least $5 : 1$ compared to fatty tissues [7, 8, 10]. The contrast between malignant lesions and fibroglandular structures seem to be highly variable, ranging between $2 : 1$ to $1.1 : 1$ [8, 9]. This contrast is caused by the higher water content in cancer tissues, which increases both their conductivity and permittivity compared to healthy breast structures. Overall, the vast majority of the studies show that the electric properties of breast tissues follow the following relationship:

$$0 < \sigma_f(\omega) \le \sigma_f^U(\omega) < \sigma_b^L(\omega) \le \sigma_b(\omega) \le \sigma_b^U(\omega) < \sigma_c^L(\omega) \le \sigma_c(\omega) \ll \infty$$
$$0 < \varepsilon_f(\omega) \le \varepsilon_f^U(\omega) < \varepsilon_b^L(\omega) \le \varepsilon_b(\omega) \le \varepsilon_b^U(\omega) < \varepsilon_c^L(\omega) \le \varepsilon_c(\omega) \ll \infty$$
$$\text{for } \omega \in [2\pi \cdot f_{\min},\ 2\pi \cdot f_{\max}] \tag{35}$$

where:

$\sigma_c(\omega) + j\omega \cdot \varepsilon_c(\omega)$ is the admittivity of the malignant breast tissue
$\sigma_f(\omega) + j\omega \cdot \varepsilon_f(\omega)$ is the admittivity of the fatty breast tissue
$\sigma_b(\omega) + j\omega \cdot \varepsilon_b(\omega)$ is the admittivity of the fibroglandular breast tissue

$\sigma_c^U(\omega)$ is the upper bound of the tumor tissues conductivity values

$\sigma_c^L(\omega)$ is the lower bound of the tumor tissues permittivity values

$\sigma_b^L(\omega)$ the lower bound of the fibroglandular tissues conductivity values

$\varepsilon_b^L(\omega)$ the lower bound of the fibroglandular tissues permittivity values

$\sigma_b^U(\omega)$ the upper bound of the fibroglandular tissues conductivity values

$\varepsilon_b^U(\omega)$ the upper bound of the fibroglandular tissues permittivity values

$\sigma_f^L(\omega)$ is the upper bound of the fatty tissues conductivity values

$\varepsilon_f^U(\omega)$ is the lower bound of the fatty tissues permittivity values

and $f_{\min}$, $f_{\max}$ are $10\,\mathrm{KHz}$ and $10\,\mathrm{GHz}$ respectively.

Consider the scenarios depicted in Figure 3. If a fixed current pattern of the same intensity, $I$, is injected in all three scenarios, it can be proven that:

$$Re\left(I \cdot Z_{\Omega_c} \cdot I^T\right) < Re\left(I \cdot Z_{\Omega_b} \cdot I^T\right) < Re\left(I \cdot Z_{\Omega_f} \cdot I^T\right) \qquad (36)$$

Using the theory presented in Section 3 and the conversion functions $\rho = \sigma/((\sigma)^2 + (\omega\varepsilon)^2)$ and $\psi = \varepsilon/\omega((\sigma)^2 + (\omega\varepsilon)^2)$, it is trivial to deduct that $Z_{\Omega_c} < Z_{\Omega_b} < Z_{\Omega_f}$. Since the electric properties of breast tissues satisfy the conditions needed to use the monotonicity principle, this reconstruction methodology seems a feasible option to reconstruct an EIT breast image. However, conventional monotonicity approaches are designed to be used in scenarios where the conducting medium is homogeneous and its use for breast imaging can therefore be problematic. The most important concern is that sometimes the monotonicity approaches can generate inaccurate estimates of the scan region. In some cases this is caused by the fact that the resistance matrix of two regions can be similar while the impedance distributions are completely different [24]. Consider the 1D example in Figure 4. The impedance does not depend on the position $x$ of the crack. Although $Z_{\Omega_1} = Z_{\Omega_2}$, the two regions are unrelated.
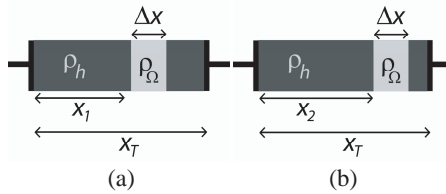


**Figure 3.** One dimensional impedance example. (a) First profile. (b) Second profile.
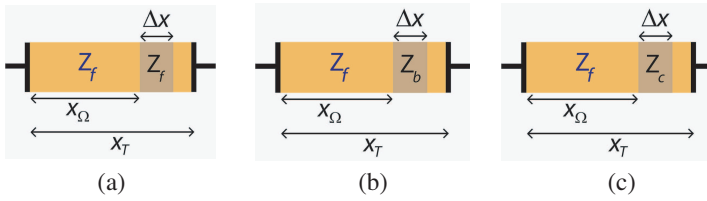
**Figure 4.** 1D breast tissue example. (a) Fatty tissue inclusion. (b) Fibroglandular inclusion. (c) Tumor inclusion.

## 4.2. EIT-BMR Reconstruction Approach

Let consider a given breast region $B$ whose impedivity is given by:

$$Z_B(x,y,\omega) \triangleq \begin{cases} \rho_f(\omega) + j \cdot \psi_f(\omega) \text{ for } (x,y) \in B \backslash \Omega_b \text{ and } r \in B \backslash \Omega_c \\ \rho_b(\omega) + j \cdot \psi_b(\omega) \text{ for } (x,y) \in \Omega_b \\ \rho_c(\omega) + j \cdot \psi_c(\omega) \text{ for } (x,y) \in \Omega_c \end{cases} \quad (37)$$

In this case, the impedivity of $B$ is also modeled as a function of the frequency to incorporate the dispersive behavior of breast tissues. To rule out impedance matrices that would yield inaccurate breast resistivity distributions, an initial estimate of the locations and dimensions of the fibroglandular and tumor regions will be incorporated to the reconstruction process. This methodology has been used successfully in the past for iterative reconstruction methods, resulting in lower execution times and improved spatial and impedivity estimation accuracy [10]. The proposed method extracts this information from BMR images since they provide a map of the tissue interfaces within the breast region. Additionally, current BMR reconstruction methods can produce accurate reflectivity maps in real time [37]. A sample BMR image and its corresponding MRI image are shown in Figure 5.

The dense tissue regions estimate is formed by performing an edge linking process over the reflectivity map $i_B(x,y)$ [38]. Then, by using the extreme values of the breast tissues resistivity and reactivity values the following estimate is defined over a discrete grid:

$$\hat{Z}_B(x,y,\omega) \begin{cases} \rho_f(\omega) + j \cdot \psi_f(\omega) \text{ for } (x,y) \in B \backslash \hat{\Omega}_b \text{ and } (x,y) \in B \backslash \hat{\Omega}_c \\ \rho_b(\omega) + j \cdot \psi_b(\omega) \text{ for } (x,y) \in \hat{\Omega}_b \\ \rho_c(\omega) + j \cdot \psi_c(\omega) \text{ for } (x,y) \in \hat{\Omega}_c \end{cases} \quad (38)$$

where $\hat{\Omega}_b$ and $\hat{\Omega}_c$ are the locations of the candidate fibroglandular and tumor regions. The candidate dense tissue regions $\hat{\Omega}_r = \hat{\Omega}_b \cup \hat{\Omega}_c$, are considered to be formed by a series of $G$ non overlapping elements, $\tau_k$, where $k = 1, 2, 3, \ldots G$. The next step is to generate a test set, $\hat{Z}_{\Omega_r \backslash \tau_n}$,
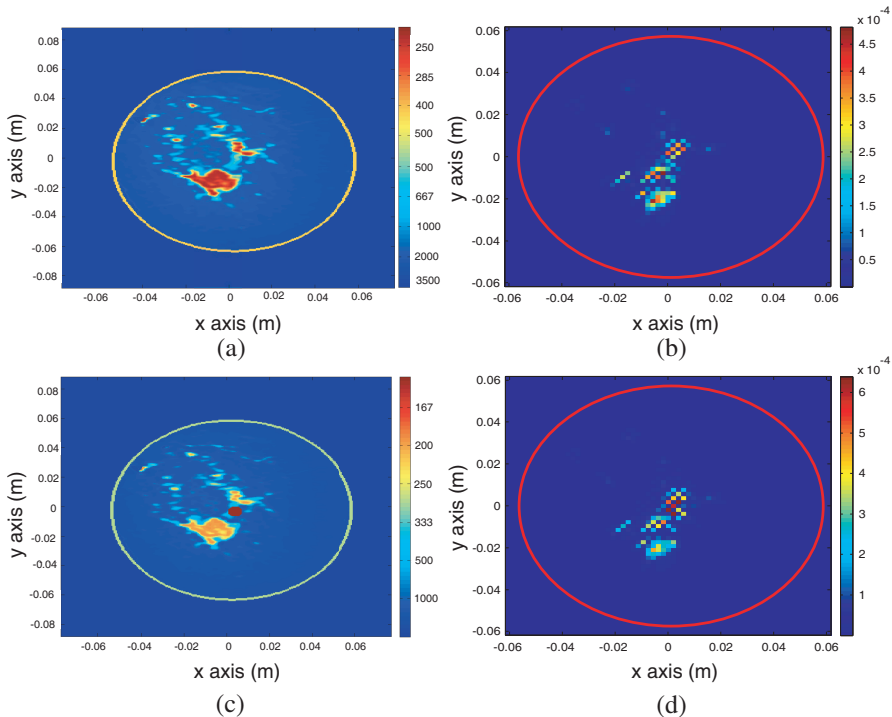
**Figure 5.** BMR image example. (a) Dielectric profile without a tumor. (b) Reconstructed BMR image. (c) Dielectric profile with a tumor. (d) Reconstructed BMR image.

to rule out the locations that do not correspond to $\Omega_b$ and $\Omega_c$. However, the noise in the measured data and/or the numerical errors in the simulation process can affect the eigenvalues of the difference matrices, yielding false estimates. To avoid this scenario, a thresholding process on the sign indices is performed. The threshold, $\varphi$, is determined by calculating the sign index of the corresponding to the element in $\hat{Z}_{\Omega_r \setminus \tau_k}$ that minimizes $\|Re(Z_D) - Re(\hat{Z}_{\Omega_n})\|^2$, where $\| \ \|$ is the norm operator. The final estimate $\Omega_{int}$ is obtained by determining the union of the elements in $\hat{Z}_{\Omega_r \setminus \tau_n}$ whose sign index is greater than $\varphi - 1$. The outcome of the proposed method is a conductivity map of the breast region. The proposed method can be summarized as follows:

1. First, the BMR data set corresponding to $B$ is collected and reconstructed, yielding the reflectivity map $i_B(x, y)$.

2. The surface responses in $i_B(x, y)$ are eliminated and an edge linking process is performed to segment the estimated

fibroglandular and tumor regions, generating $\hat{Z}_B(x, y)$.

3. A grid inside the scan region is defined. This grid is formed by square cells of length is $l$.

4. The set of test matrices, $\hat{Z}_{\Omega_r \backslash \tau_n}$, is then simulated. $\hat{Z}_{\Omega_r \backslash \tau_n}$ is defined as follows:

$$\hat{Z}_{\Omega_r \backslash \tau_n} = \left\{ \hat{Z}_{\Omega_r \backslash \tau_1}, \hat{Z}_{\Omega_r \backslash \tau_1}, \hat{Z}_{\Omega_r \backslash \tau_2}, \hat{Z}_{\Omega_r \backslash \tau_3} \ldots \hat{Z}_{\Omega_r \backslash \tau_N} \hat{Z}_{\Omega_r \backslash \tau_N} \right\} \quad (39)$$

5. The sign index of $Re(Z_B) - Re(\hat{Z}_{\Omega_r \backslash \tau_n})$, $s_n$, is then calculated for all the test matrices. This index is defined as:

$$s_n = \frac{\Sigma_j \lambda_{n,j}}{\Sigma_j |\lambda_{n,j}|} \quad (40)$$

where $\lambda_{n,j}$ is the $j$th eigenvalue of $Re(Z_B) - Re(\hat{Z}_{\Omega_r \backslash \tau_n})$.

6. The noise present in the measured data can corrupt the eigenvalues of $Re(Z_B) - Re(\hat{Z}_{\Omega_r \backslash \tau_n})$ and consequently the value of $t_n$. The effect of noise on $s_n$ is harmful because it can be responsible for
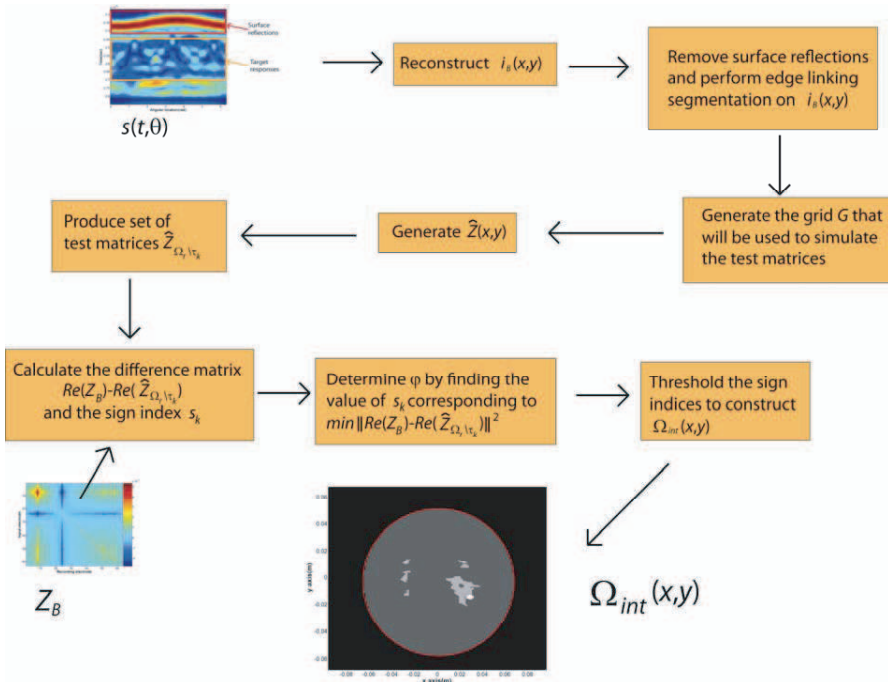


**Figure 6.** Flow diagram of the proposed method.

excluding spatial locations from the final reconstructed profile [24]. To compensate this effect, the following threshold is calculated:

$$\varphi \triangleq \left\{ \frac{\Sigma_j \lambda_{\varphi,j}}{\Sigma_j |\lambda_{\varphi,j}|} \,|\, \arg\min \left\| Re(Z_B) - Re\left(\hat{Z}_{\Omega_\varphi}\right) \right\|^2, \hat{Z}_{\Omega_\varphi} \in \hat{Z}_{\Omega_r \setminus \tau_n} \right\} \quad (41)$$

where $\varphi \in [-1, 0]$, $\lambda_{\varphi,j}$ are the eigenvalues of $Re(Z_B) - Re(\hat{Z}_{\Omega_\varphi})$.

7. The final reconstructed profile is defined as:

$$\Omega_{int} \triangleq \cup_{n \in I_{int}} s_n \qquad\qquad\qquad (42)$$

$$I_{int} \triangleq \left\{ Re\left(\hat{Z}_{\Omega_r \setminus \tau_n}\right) | \varphi - 1 < s_n, \; n = 1, 2, 3 \ldots N \right\} \quad (43)$$

Note that in scenarios where no disturbances are present, the criterion would become $-1 < s_n$ which is essentially all the scenarios that are not negatively well defined. A flow diagram of the proposed method can be seen in Figure 6.

## 5. RESULTS

To evaluate the performance of the proposed method, four numerical breast phantoms were used. These breast phantoms were generated using breast MRI images obtained from the University of Wisconsin-Madison online repository. The tissue type and water content of the different intensities on the MRI images were obtained using the process outlined in the repository webpage. All the images used in this study are an axial view from the mid section level (3–4 cm from the chest wall) of an ACR2 type breast from a patient with average breast density.

An EIT and a BMR datasets were simulated for each testbed. The electric properties of the different breast tissues in the EIT and BMR datasets were based on the values published in [3, 4, 7] and [8] respectively. The EIT datasets were simulated using the FEM engine included in Quickfield 5.1 (Tera Analysis Inc.). The breast regions were surrounded by sixty-four 1 mm electrodes, arranged in a circular pattern. A sinusoid current pattern with an amplitude of 5 mA and a frequency of 55 KHz was applied. The original EIT data sets were simulated using a grid that had a cell size of 500 µm. To avoid the inverse crime, the cell size used during to simulate the test matrices was 1 mm, according to the criteria described in [30]. White noise with a zero mean and an average variance of 0.2 mV was added to the simulated data sets. A tumor with a diameter of 6 mm was included in all datasets. The tumor dimensions and locations in all the testbeds were chosen to mimic the position and sizes of non-palpable lesions in realistic scenarios [39]. The BMR data sets were produced using a radar simulator developed by the authors [40]. This simulation

suite is based on the first order Born approximation of a monostatic radar signal and has been tested by the authors using finite difference time domain approach and experimental radar datasets from synthetic breast phantoms, yielding promising results. The BMR scan geometry had 72 scan equally spaced locations around a circle with a 18 cm radius in the $(x, y)$ plane. A Vivaldi antenna with length of 11 cms was modeled as the irradiating element. The same MRI data sets were used to generate the corresponding BMR numeric phantoms. A Stepped Frequency Continuous Wave (SFCW) was irradiated in each scan location. The SCFW had a bandwidth of 11 GHz with a center frequency of 6.5 GHz. The proposed method was implemented in a desktop PC with a 2.6 GHz Phenom 9950 Quad CPU and 8 GB RAM. To allow a better display of the breast structures in the reconstructed BMR images, the skin responses were located and removed using the algorithm proposed by the authors in [41]. A red contour is instead used to indicate the location of skin. In all the BMR images, the energy of the reconstructed responses is shown. Since the bimodal reconstruction method assigns every region in the conducting domain into one of the main types of tissues, the images generated by the proposed approach are shown in four colors: dark gray for fatty tissues, light gray for fibroglandular,white for tumor and black for the background material.

The spatial accuracy of the proposed method was evaluated by determining the dimension and location errors of the tumors in the reconstructed images. Additionally, the area overlap between the reconstructed images and the original testbeds were evaluated using the Dice Similarity Coefficient (DSC). This metric is defined as:

$$\mathrm{DSC} = \frac{A \cap B}{2(A + B)} \tag{44}$$

where $A$ are the regions manually segmented by an expert and $B$ are the regions generated by the proposed method. A DSC of 1 indicates a perfect agreement in dimensions and locations between the objects under evaluation. This metric was calculated for both the fibroglandular areas and the cancerous regions.

An initial MRI testbed and the results of the proposed method on its corresponding datasets are shown in Figure 7. This testbed consist of a several fibroglandular regions and a tumor located at in the middle. This is a quite challenging scenario for BMR since the responses from the fibroglandular region and the tumor will likely have comparable magnitudes, making an accurate assessment of the tumor presence a difficult task. Notice how the BMR image gives a rough illustration of the reflectivity of the scan region and that there are a number of extra locations that also have a high reflectivity, such as

the lower region of the fibroglandular area. The results of the joint approach are shown in Figure 7(c). The edges in the resulting image can be clearly appreciated and the location of the tumor is well defined and consistent with its location on the simulated testbed, as indicated by its DSC, spatial and area errors (0.98, (0.5, 0.7) mm and $3\,\text{mm}^2$ respectively). Note also that the different nature of the tumor can be distinguished from the surrounding fibroglandular region, contrary to the BMR image, allowing a more accurate diagnosis. The DSC value for the fibroglandular regions was 0.92.

A second testbed is shown in Figure 8(a). In this case, the breast region includes a large fibroglandular area (3 cm major diameter, 2.5 cm minor diameter) with a tumor attached to its lower end. Small portions of fibroglandular tissue are present in the upper and mid region of the breast region as well. Figure 8(b) shows the reconstructed BMR image. Notice that the predominant response comes from the tumor
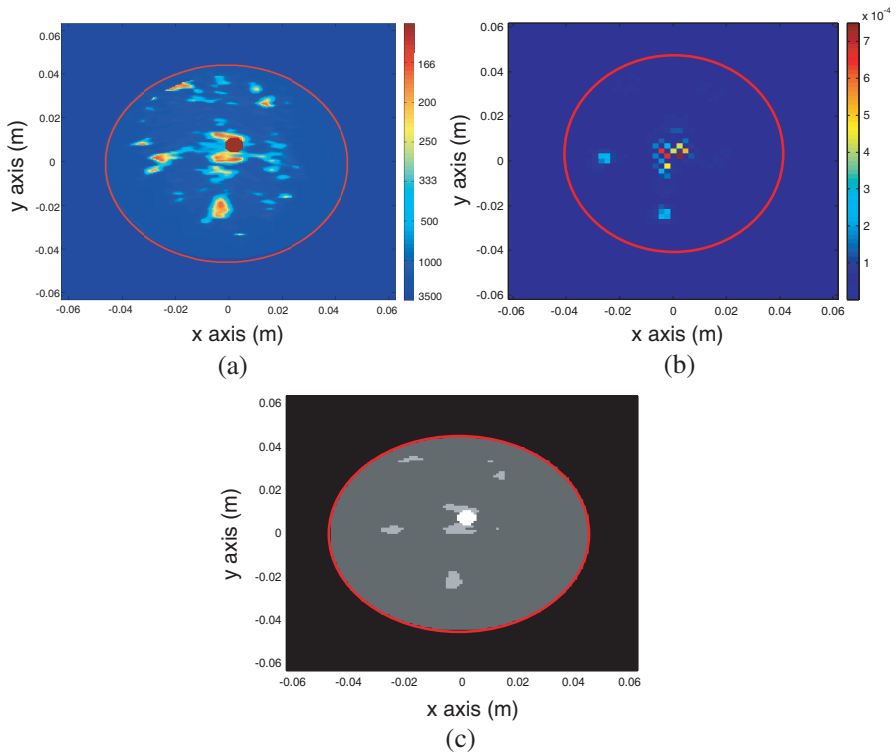


**Figure 7.** Experiment 1. (a) Numeric testbed. (b) Reconstructed BMR image. (c) Image produced by the proposed method.

location, but a radar signature with considerable energy $(3.7 \times 10^{-4}$ watts) is located 2.5 cm above it. This response corresponds to the location of a sharp corner reflector at the top of the fibroglandular patch. The image generated by the proposed approach is shown in Figure 8(c). Notice how the presence of tumor location is consistent with its location on the testbed, and how it is easier to distinguish the difference between the sharp corner reflectors since they appear as fibroglandular tissue. Although some of the smaller fibroglandular regions do not appear in the reconstructed image, the main dense tissue region and the tumor can be clearly identified. The reason why these regions did not appear in the final is mostly because they had responses with magnitudes similar to noise levels in the BMR datasets. The tumor location and area errors in the image produced by the proposed approach were $(-1, 1)$ mm and $13 \, \text{mm}^2$ respectively. The DSC values for the tumor and fibroglandular regions were 0.8824 and 0.9181.
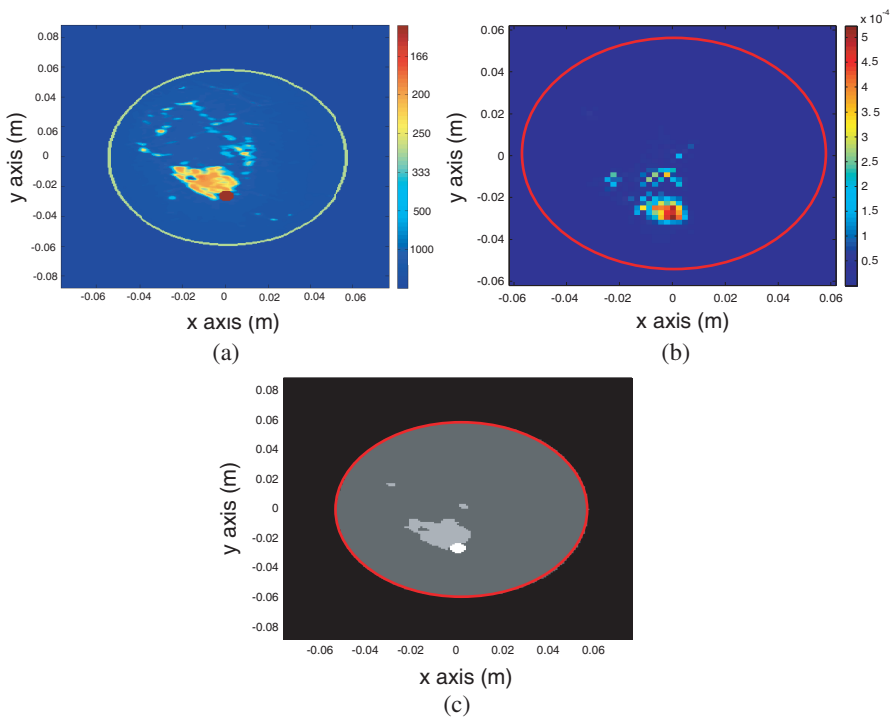


Figure 8. Experiment 2. (a) Numeric testbed. (b) Reconstructed BMR image. (c) Image produced by the proposed method.

A third numeric phantom is shown in Figure 9(a). In this case, the breast region also has a large fibroglandular patch at its lower half, with a tumor attached at its top end. This is a challenging scenario for BMR imaging, as the fibroglandular region tends to obscure the reflections from the tumor. As it can observed in Figure 9(b), there are two main responses in the BMR reconstructed image. Notice how the largest response corresponds to the lower end of the fibroglandular region. Additionally, the response on the top of the fibroglandular area has a magnitude comparable to the tumor response. These additional responses make difficult to identify the presence and location of the tumor in the BMR image. The results of the proposed algorithm are shown in Figure 9(c). Note how the tumor can be clearly identified and its location is consistent with its position in the testbed. Similarly to the results of the previous numeric phantom, some of the small fibroglandular regions were not reconstructed properly, although the large dense tissue regions and the malignant lesion are clearly
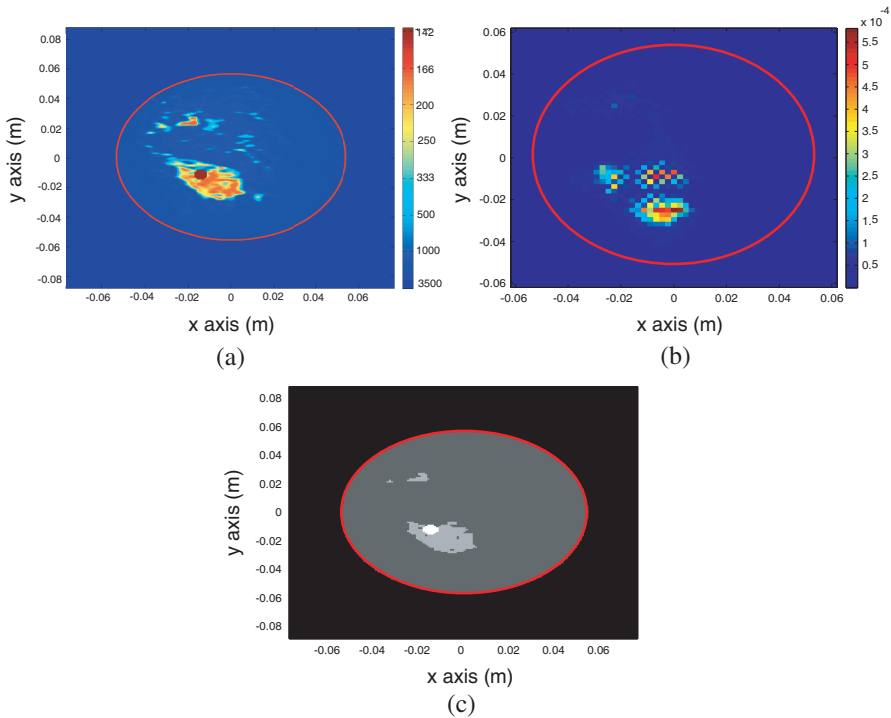


**Figure 9.** Experiment 3. (a) Numeric testbed. (b) Reconstructed BMR image. (c) Image produced by the proposed method.

identifiable. The tumor location and area errors in the image produced by the bimodal technique were $(-0.3, 0.9)$ mm and $3\,\mathrm{mm}^2$ respectively. The DSC values for the tumor and fibroglandular regions were 0.81 and 0.99.

A fourth testbed and its corresponding images are displayed in Figure 10. This numeric phantom has a smaller, but more spiculated fibroglandular region that the previous three cases. As it can be seen in Figure 10(b), the additional corner reflectors yield high magnitude responses that can obscure the reflections from the tumor. In specific, the dominant responses in the image correspond to the upper-right interface of the fibroglandular region. The lower-left interface also presents a significant response, which has a higher magnitude than the tumor radar signature. These high magnitude responses in the BMR image difficult the detection of the tumor present in the breast region. The results of the proposed method are shown in Figure 10(c). Notice how the tumor can be clearly distinguished in the image
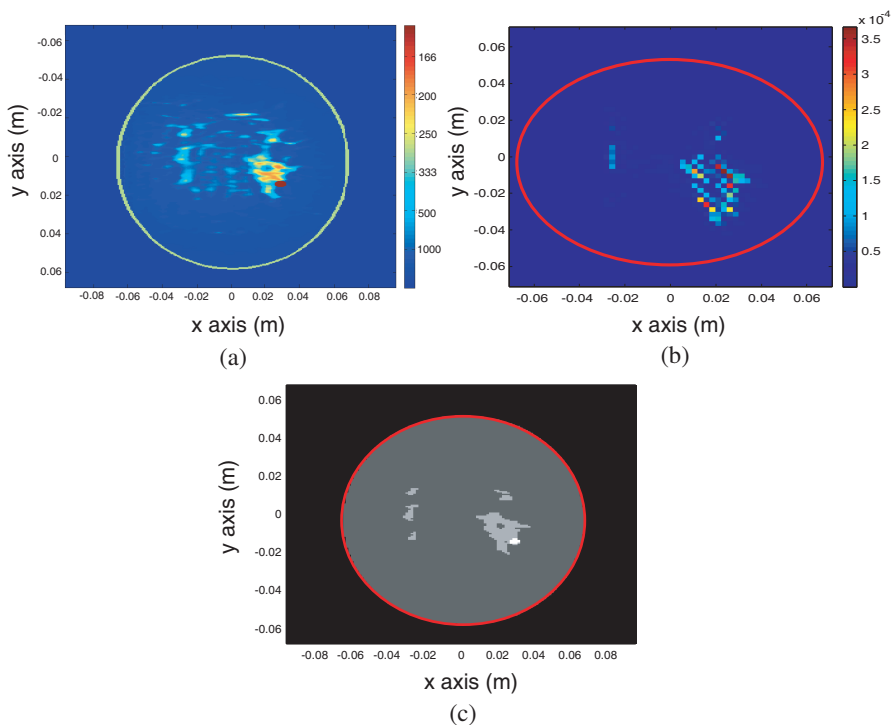


**Figure 10.** Experiment 4. (a) Numeric testbed. (b) Reconstructed BMR image. (c) Image produced by the proposed method.

**Table 1.** Location and area errors for the reconstructed datasets.

| Dataset | Location error | Area error |
|:---:|:---:|:---:|
| 1 | $(0.5, 0.7)$ mm | $3\,\mathrm{mm}^2$ |
| 2 | $(-1, 1)$ mm | $13\,\mathrm{mm}^2$ |
| 3 | $(-0.3, 0.9)$ mm | $2\,\mathrm{mm}^2$ |
| 4 | $(1, -1.5)$ mm | $8\,\mathrm{mm}^2$ |

**Table 2.** DSC values for the reconstructed datasets.

| Experiment | DSC fibroglandular regions | DSC tumor regions |
|:---:|:---:|:---:|
| 1 | 0.92 | 0.98 |
| 2 | 0.9181 | 0.8824 |
| 3 | 0.81 | 0.99 |
| 4 | 0.9589 | 0.9118 |

generated by the proposed method, when compared to the BMR image. Additionally, location and dimension of the main fibroglandular region and the tumor in the image produced by the bimodal approach are consistent with its position in the testbed as shown by the DSC values (0.9118 for the tumor and 0.9589 for the fibroglandular area). The tumor location and area errors in the image produced by the proposed approach were $(1, -1.5)$ mm and $8\,\mathrm{mm}^2$ respectively. The error and DSC values for all the experiments are summarized in Table 1 and Table 2 respectively.

## 6. CONCLUSIONS

In this paper, a novel bimodal EMI image formation technique was presented. This technique combines both BMR and EIT methods to form a resistivity distribution map of a breast region that can be used to assess the presence of malignant lesions. The proposed approach generates an estimate of the dense tissue regions using the BMR image of the breast while accurately preserving the borders between dense and fatty regions. This estimate is then used to initialize an EIT reconstruction method based on the monotonicity principle. The proposed technique yielded very promising results when applied to MRI-derived numeric phantoms. Although some of the smaller dense tissue regions did not appear on the reconstructed images, all simulated tumors were successfully located. Additionally, the performance of the proposed method was quantitatively assessed yielding spatial errors of less than 4 mm and DSC values over 0.9 for fibroglandular tissue

regions and 0.85 for malignant lesions. Future research will be focused on developing a multimodal data acquisition system that will be used to assess the experimental feasibility of this algorithm.

# REFERENCES

1. *Cancer Facts & Figures*, American Cancer Society, Atlanta, 2009.
2. Flöry, D., M. W. Fuchsjaeger, C. F. Weisman, and T. H. Helbich, "Advances in breast imaging: A dilemma or progress," *Minimally Invasive Breast Biopsies*, Vol. 173, 159–181, 2009.
3. Poplack, S. P., K. D. Paulsen, A. Hartov, P. M. Meaney, B. Pogue, T. Tosteson, M. Grove, S. Soho, and W. Wells, "Electromagnetic breast imaging: Pilot results in women with abnormal mammograms," *Radiology*, Vol. 243, 350–359, 2007.
4. Kerner, T. E., K. D. Paulsen, A. Hartov, S. K. Soho, and S. P. Poplack, "Electrical impedance spectroscopy of the breast: Clinical imaging results in 26 subjects," *IEEE Transactions on Medical Imaging*, Vol. 21, 638–645, June 2002.
5. Meaney, P. M., M. W. Fannin, T. Raynolds, C. J. Fox, Q. Fang, C. A. Kogel, S. P. Poplack, and K. D. Paulsen, "Initial clinical experience with microwave breast imaging in women with normal mammography," *Academic Radiology*, Vol. 14, 207–218, 2007.
6. Klemm, M., J. A. Leendertz, D. Gibbins, I. J. Craddock, A. Preece, and R. Benjamin, "Microwave radar-based breast cancer detection: Imaging in inhomogeneous breast phantoms," *IEEE Antennas and Wireless Propagation Letters*, available online, December 2009.
7. Jossinet, J., "Variability of impedivity in normal and pathological breast tissue," *Medical and Biological Engineering and Computing*, Vol. 34, 346–350, September 1996.
8. Lazebnik, M., L. McCartney, D. Popovic, C. B. Watkins, M. J. Lindstrom, J. Harter, S. Sewall, A. Magliocco, J. H. Booske, M. Okoniewski, and S. C. Hagness, "A large-scale study of the ultrawideband microwave dielectric properties of normal breast tissue obtained from reduction surgeries," *Physics in Medicine and Biology*, Vol. 52, 2637–2656, April 2007.
9. Halter, R. J., T. Zhou, P. M. Meaney, A. Hartov, R. Barth, K. Rosenkranz, W. Wells, C. Kogel, A. Borsic, E. Rizzo, and K. D. Paulsen, "The correlation of in vivo and ex vivo tissue dielectric properties to validate electromagnetic breast imaging: Initial clinical experience," *Physiological Measurement*, Vol. 30, 121–136, 2009.

10. Surowiec, S. J., S. S. Stuchly, J. R. Barr, and A. Swarup, "Dielectric properties of breast carcinoma and the surrounding tissues," *IEEE Transactions on Biomedical Engineering*, Vol. 35, 257–263, April 1988.

11. Fear, E. C. and M. A. Stuchly, "Microwave detection of breast cancer," *IEEE Transactions on Microwave Theory and Techniques*, Vol. 48, 1854–1863, November 2000.

12. Klemm, M., I. J. Craddock, J. A. Leendertz, A. Preece, and R. Benjamin, "Radar-based breast cancer detection using a hemispherical antenna array — Experimental results," *IEEE Transactions on Antennas and Propagation*, Vol. 57, 1692–1704, June 2009.

13. Flores-Tapia, D., G. Thomas, and S. Pistorius, "A wavefront reconstruction method for 3D cylindrical subsurface radar imaging," *IEEE Transactions on Image Processing*, Vol. 17, 1908–1925, October 2008.

14. Klemm, M., I. J. Craddock, J. A. Leendertz, A. Preece, D. R. Gibbins, M. Shere, and R. Benjamin, "Clinical trials of a UWB imaging radar for breast cancer," *2010 Proceedings of the Fourth European Conference on Antennas and Propagation*, 1–4, April 2010.

15. Salvador, S. M. and G. Vecchi, "Experimental tests of microwave breast cancer detection on phantoms," *IEEE Transactions on Antennas and Propagation*, Vol. 57, 1705–1712, June 2009.

16. Mashal, A., J. H. Booske, and S. C. Hagness, "Toward contrast-enhanced microwave-induced thermoacoustic imaging of breast cancer: An experimental study of the effects of microbubbles on simple thermoacoustic targets," *Physics in Medicine and Biology*, Vol. 54, 641–650, 2009.

17. Mashal, A., B. Sitharaman, X. Li, P. K. Avti, A. V. Sahakian, J. H. Booske, and S. C. Hagness, "Toward carbon-nanotube-based theranostic agents for microwave detection and treatment of breast cancer: Enhanced dielectric and heating response of tissue-mimicking materials," *IEEE Transactions on Biomedical Engineering*, Vol. 57, 1831–1834, August 2010.

18. Chen, Y. F., I. J. Craddock, and P. Kosmas, "Feasibility study of lesion classification via contrast-agent-aided UWB breast imaging," *IEEE Transactions on Biomedical Engineering*, Vol. 57, No. 5, 1003–1007, May 2010.

19. Rubaek, T., P. M. Meaney, P. Meincke, and K. D. Paulsen, "Nonlinear microwave imaging for breast cancer screening using Gauss–Newton's method and the CGLS inversion algorithm,"

*IEEE Transactions on Antennas and Propagation*, Vol. 55, 2320–2331, August 2007.

20. Demidenko, E., A. Hartov, and K. Paulsen, "Statistical estimation of resistance/conductance by electrical impedance tomography measurements," *IEEE Transactions on Medical Imaging*, Vol. 23, 829–838, July 2004.

21. Hartov, A., R. A. Mazzarese, F. R. Reiss, T. E. Kerner, K. S. Osterman, D. B. Williams, and K. D. Paulsen, "A multichannel continuously selectable multifrequency electrical impedance spectroscopy measurement system," *IEEE Transactions on Biomedical Engineering*, Vol. 47, 49–58, January 2000.

22. Cherepenin, V. A., A. Y. Karpov, A. V. Korjenevsky, V. N. Kornienko, Y. S. Kultiasov, M. B. Ochapkin, O. V. Trochanova, and J. D. Meister, "Three-dimensional EIT imaging of breast tissues: System design and clinical testing," *IEEE Transactions on Medical Imaging*, Vol. 21, 662–667, June 2002.

23. Boverman, G., T.-J. Kao, R. Kulkarni, B. S. Kim, D. Isaacson, G. J. Saulnier, and J. C. Newell, "Robust linearized image reconstruction for multifrequency eit of the breast," *IEEE Transactions on Medical Imaging*, Vol. 27, 1439–1448, October 2008.

24. Tamburrinoand, A. and G. Rubinacci, "A new non-iterative inversion method for electrical resistance tomography," *Inverse Problems*, Vol. 18, 1809–1829, December 2002.

25. Flores-Tapia, D. and S. Pistorius, "Electrical impedance tomography reconstruction using a monotonicity approach based on a priori knowledge," *2010 Annual International Conference of the IEEE Engineering in Medicine and Biology Society (EMBC)*, 4996–4999, August–September 2010.

26. Conceicao, R., M. O'Halloran, M. Glavin, and E. Jones, "Comparison of planar and circular antenna configurations for breast cancer detection using microwave imaging," *Progress In Electromagnetics Research*, Vol. 99, 1–20, 2009.

27. Soumekh, M., *Synthetic Aperture Radar Signal Processing with MATLAB Algorithms*, Wiley-Interscience, New York City, New York, USA, 1999.

28. Bayford, R. H., "Bioimpedance tomography," *Annual Review of Biomedical Engineering*, Vol. 8, 63–91, August 2006.

29. Holder, D. S., *Electrical Impedance Tomography: Methods, History and Applications*, IOP Publishing, Bristol, UK, 2005.

30. Neumaier, A., "Solving Ill-conditioned and singular linear systems: A tutorial on regularization," *SIAM Review*, Vol. 40,

636–666, September 1998.

31. Marquadt, D., "An algorithm for least squares estimation of nonlinear parameters," *SIAM Journal of Applied Mathematics*, Vol. 11, 431–441, June 1963.

32. Vogel, C., *Computational Methods for Inverse Problems*, SIAM, Philadelphia, PA, USA, 2001.

33. Somersalo, E., M. Cheaney, D. Issacson, and E. Issacson, "Layer stripping, a direct numerical method for impedance imaging," *Inverse Problems*, Vol. 7, 899–926, December 1991.

34. Siltaten, S., J. Mueller, and D. Issacson, "An implementation of the reconstruction algorithms of Nachman for the 2D inverse conductivity problem," *Inverse Problems*, Vol. 16, 681–699, June 2000.

35. Bruhl, M., "Explicit characterization of inclusions in electrical impedance tomography," *SIAM Journal on Mathematical Analysis*, Vol. 32, 1327–1341, December 2001.

36. Yaffe, M. J., J. M. Boone, N. Packard, O. Alonzo-Proulx, S. Y. Huang, C. L. Peressotti, A. Al-Mayah, and K. Brock, "The myth of the 50-50 breast," *Medical Physics*, Vol. 36, 5437–5443, December 2009.

37. Flores-Tapia, D. and S. Pistorius, "A real time wavefront reconstruction approach for breast microwave imaging using SMPD based interpolation," *IEEE 2010 International Conference on Image Processing*, October 2010.

38. Gonzalez, R. C. and R. E. Woods, *Digital Image Processing*, Prentice Hall, Upper Saddle River, New Jersey, USA, 2002.

39. Hughes, L. L., M. Wang, D. L. Page, R. Gray, L. J. Solin, N. E. Davidson, M. A. Lowen, J. N. Ingle, A. Recht, and W. C. Wood, "Local excision alone without irradiation for ductal carcinoma in situ of the breast: A trial of the Eastern Cooperative on Cology Group," *Journal of Clinical Oncology*, Vol. 27, 5319–5324, November 2009.

40. Flores-Tapia, D., G. Thomas, A. Sabouni, S. Noghanian, and S. Pistorius, "Breast tumor microwave simulator based on a radar signal model," *IEEE International Symposium on Signal Processing and Information Technology*, 1–6, August 2006.

41. Flores-Tapia, D., G. Thomas, and S. Pistorius, "Skin surface removal on breast microwave imagery," *Proceedings of the SPIE Medical Imaging 2006 Conference*, Vol. 7, No. 2, 61433A.1–61433A.9, February 2006.